CCFE
CULHAM CENTRE FOR FUSION ENERGY

UK Atomic Energy Authority

UKAEA-CCFE-PR(23)129

H. J. C. Oliver, S. E. Sharapov, Z. Stancar, M. Fitzgerald, E. Tholerus, B. N. Breizman, M. Dreval, J. Ferreira, A. Figueiredo, J. Garcia, N. Hawkes, D. L. Keeling, P. G. Puglia, P. Rodrigues, A. Tinguely, JET contributors

Toroidal Alfven eigenmodes observed in low power JET deuterium-tritium plasmas

Toroidal Alfven eigenmodes observed in low power JET deuterium-tritium plasmas

H. J. C. Oliver, S. E. Sharapov, Z. Stancar, M. Fitzgerald, E. Tholerus, B. N. Breizman, M. Dreval, J. Ferreira, A. Figueiredo, J. Garcia, N. Hawkes, D. L. Keeling, P. G. Puglia, P. Rodrigues, A. Tinguely, JET contributors

This is a preprint of a paper submitted for publication in Nuclear Fusion

Toroidal Alfvén eigenmodes observed in low power JET deuterium-tritium plasmas

H. J. C. Oliver[1], S. E. Sharapov[1], Ž. Štancar[1], M. Fitzgerald[1], E. Tholerus[1], B. N. Breizman[2], M. Dreval[3], J. Ferreira[4], A. Figueiredo[4], J. Garcia[5], N. Hawkes[1], D. L. Keeling[1], P. G. Puglia[6], P. Rodrigues[4], A. Tinguely[7], and JET contributors[*]

[1]United Kingdom Atomic Energy Authority, Culham Centre for Fusion Energy, Culham Science Centre, Abingdon, Oxon, OX14 3DB, UK
[2]Institute for Fusion Studies, University of Texas at Austin, Austin, Texas 78712, USA
[3]National Science Centre, Kharkiv Institute of Physics and Technology, 61108 Kharkiv, Ukraine
[4]Instituto de Plasmas e Fusão Nuclear, Instituto Superior Técnico, Universidade de Lisboa, Portugal
[5]CEA, IRFM, 13108 Saint-Paul-Lez-Durance, France
[6]Ecole Polytechnique Fédérale de Lausanne, Swiss Plasma Center, CH-1015 Lausanne, Switzerland
[7]Plasma Science and Fusion Center, Massachusetts Institute of Technology, Cambridge, Massachusetts 02139, USA

[*]See the author list of 'Overview of JET results for optimising ITER operation' by J. Mailloux et al 2022 Nucl. Fusion 62 042026

Abstract

The Joint European Torus (JET) recently carried out an experimental campaign using a plasma consisting of both deuterium (D) and tritium (T). We observed high-frequency modes using a reflectometer and an interferometer in a DT plasma heated with low power neutral beam injection, $P_{NBI} = 11.6\ MW$. These modes were observed at a frequency $f = 156\ kHz$, were located deep in the plasma, and exhibited frequency chirping. The observed modes were identified as toroidal Alfvén eigenmodes (TAEs) using the linear MHD code, MISHKA. The stability of 21 modes that match experimental measurements was investigated. Beam ions and fusion-born alpha particles were modelled using the full orbit particle tracking code LOCUST. LOCUST exploits GPU hardware to follow $\sim 10^7$ particles from birth to thermalisation, producing a smooth distribution function suitable for stability calculations without analytical fits or the use of moments. At least 6M beam markers were required to capture all of the crucial features of the distribution function in sufficient detail. We calculated the stability of the 21 candidate modes using the HALO code, which models the wave-particle interaction. These calculations revealed that beam ions can drive TAEs with toroidal mode numbers $n \geq 8$ with linear growth rates $\gamma_d/\omega \sim 1\%$, while TAEs with $n < 8$ are damped by the beam ion population. This finding was supported by a simple analytical model. Alpha particles drive modes with significantly smaller linear growth rates, $\gamma_\alpha/\omega \lesssim 0.1\%$ due to the low alpha power generated almost exclusively by beam-thermal fusion reactions. At least 4M beam ions and 1M alpha particles were required in HALO to represent the distribution function. Guiding centre calculations were found to significantly over-estimate growth rates compared to full orbit calculations for both beam ions and alpha particles. Non-ideal effects were calculated using complex resistivity in the CASTOR code, leading to an assessment of radiative, collisional, and continuum damping for all 21 candidate modes. Ion Landau damping was modelled using Maxwellian distribution functions for bulk D and T ions in HALO. Radiative damping, the dominant damping mechanism, suppresses modes with high toroidal mode numbers. Collisional damping was also significant, particularly for modes in the outer half of the plasma. Comparing the drive from energetic particles with damping from thermal particles, we find all but one of the candidate modes are damped. The single net-driven $n = 9$ TAE with a net growth rate $\gamma/\omega = 0.02\%$ matches experimental observations with a lab frequency $f = 163kHz$, location $R = 3.31m$ and marginal instability. The TAE was driven by co-passing particles through the $v_\parallel = v_A/5$ resonance, with additional sideband resonances contributing

significant drive. A beam-driven mode is observed in our experiment due to low damping caused by the weak electron temperature and high magnetic field.

1 Introduction

Toroidal Alfvén eigenmodes (TAEs) [1] are weakly damped modes of plasma oscillation that can be excited by populations of fast ions in tokamak plasmas. TAEs have been studied extensively due to their ability to transport energetic particles. Redistribution of fast ions degrades fusion reactor performance and can potentially damage the first wall of a tokamak if sufficient numbers of energetic particles are moved onto unconfined orbits during the interaction with the TAE. The amplitude of a TAE resonating with a population of energetic particles will evolve with the linear growth rate,

$$\frac{\gamma}{\omega} \approx \omega \frac{\partial f}{\partial E} + n \frac{\partial f}{\partial P_\phi}, \tag{1}$$

where n is the toroidal mode number, ω is the eigenfrequency, and $f(\sigma, E, \mu, P_\phi)$ is the energetic particle distribution function. The distribution function depends on the direction of parallel motion relative to the plasma current $\sigma = sign(v_\parallel)$, the particle energy E, the magnetic moment μ, and the canonical toroidal angular momentum $P_\phi = m_j R v_\phi + e_j \Psi$, which depends on the particle mass m_j, charge e_j, major radius R, toroidal velocity v_ϕ, and poloidal flux Ψ. We have neglected the free energy source associated with gradients in the magnetic moment, which can only drive waves with frequencies close to or above the ion cyclotron frequency ω_{ci}. Equation 1 is often rewritten in terms of the ion diamagnetic frequency [2]:

$$\omega_* = \frac{\partial f}{\partial P_\phi} \Big/ \frac{\partial f}{\partial E} \tag{2}$$

to obtain the condition for instability: $n\omega_* > \omega$. This energy can be readily accessed if the wave resonates with an energetic ion with characteristic poloidal and toroidal frequencies of motion, $\langle \dot{\theta} \rangle$ and $\langle \dot{\phi} \rangle$, that satisfy the resonance condition [2]:

$$\omega + n\langle \dot{\phi} \rangle + p\langle \dot{\theta} \rangle = 0, \tag{3}$$

where p is an integer. Energetic ions are introduced by auxiliary heating schemes, such as neutral beam injection (NBI) and ion cyclotron resonance heating (ICRH). In plasmas composed of deuterium and tritium, appreciable numbers of fusion-born alpha particles may also be present. The stability of Alfvén eigenmodes (AEs) due to interactions with these fast particles is routinely calculated numerically using two different methods of approximating the fast particle distribution function. Both approaches remove spurious gradients introduced by noise, and therefore erroneous drive or damping, by reducing the fidelity of the model.

The simplest approach approximates the distribution function using analytical expressions. The energy and spatial distribution can be assumed to follow the slowing down distribution function [3, 4]. The dependence on pitch angle $\lambda = v_\parallel / v$ or the pitch invariant $\Lambda = \mu B_0 / E$ is either neglected by assuming isotropy or approximated as a Gaussian function. These functions are combined by assuming the variables are independent and the distribution function is separable. More physics can be added by using analytical fits or moments of distribution functions generated by Monte Carlo codes, which follow the motion of the full orbit or guiding centre orbit of fast particles in a tokamak. Fits of the Monte Carlo generated distribution function itself (e.g. [5]) retain finite orbit and anisotropic effects. However, this method

smooths over important features of the distribution function in order to remove the impact of noise or poor numerical convergence on the stability calculation [6].

In this study, we exploit the full capability of a Monte Carlo code by retaining the resultant distribution function without fitting the distribution function or using moments in the stability calculation. This technique was previously unreliable due to statistical noise, but the use of GPU hardware enables the calculation of high-resolution, smooth distribution functions required for stability calculations. Thereby, we retain critical features of the distribution function, including the trapped-passing boundary, the full, half and third energy injection of the beam, and the complex inter-dependencies of the constants of motion. We used the Monte Carlo code LOCUST to generate high-resolution, smooth distribution functions. These distribution functions were used in the HALO code, which models wave-particle interactions, to assess the stability of several candidate modes. Thereby, we identified a single net-driven TAE that matched experimental observations from our DT experiment. This new technique revealed the conditions required for modes to be driven unstable by beam ions, which were previously considered to heavily damp TAEs in JET [7, 8, 9].

2 Experimental observations

We designed an experiment to generate a bump-on-tail energy distribution in the alpha particle population. Positive gradients in energy were produced by modulating the beam power on timescales shorter than the alpha particle slowing down time. The experiment aimed to excite Alfvén eigenmodes with these positive energy gradients (through the first term in Equation 1). ICRH was absent to remove any ambiguity around the source of drive for observed modes. However, modes were observed before the beam modulation began. In this paper, we focus on modes excited at time $t = 7.55\ s$ in JET pulse #99503. A discussion of other experimental results can be found in Reference [10].

The equilibrium magnetic field, $B_0 = 3.7\ T$, was relatively high and the plasma current was relatively low, $I_p = 2.5\ MA$, for JET. The time evolution of important plasma parameters is depicted in Figure 1. At the time of interest, the fusion yield reaches $4.22 \times 10^{17}\ s^{-1}$ (first frame), which was near the peak value of $4.45 \times 10^{17}\ s^{-1}$. The fusion yield was dominated by beam-thermal fusion reactions, which are strongly dependent on the deuterium beam power (second frame), $P_{NBI}(t = 7.55s) = 11.6MW$, and the D/T mix of the plasma (third frame), $D : T(t = 7.55s) = 35 : 63\%$ with the rest of the ion mix composed of Beryllium and Tungsten impurities. The reaction rate was modest for a DT experiment due to the low beam power, producing $1.19\ MW$ of fusion power, or $240\ kW$ of alpha power, corresponding to a fusion gain of $Q = 0.1$.

The presence of edge localised modes (ELMs) in the radiated power signal (second frame of Figure 1) shows the plasma in H-mode at the time of interest. Approximately half of the beam power was radiated away, due to impurity accumulation exacerbated by the absence of ICRH. This high radiated fraction causes the electron temperature in the core to become hollow, $T_e(3.11m) > T_e(3.07m) > T_e(2.93m)$, which is visible in the final frame of Figure 1.

Figure 2 shows the spectrograph of the density perturbation measured by a fast far-infrared interferometer [11]. A mode can be observed at a frequency $f = 156\ kHz$ at time $t = 7.55\ s$. A closer inspection of the modes observed in the interferometer signal reveals chirping behaviour, with the mode frequency sweeping down from $156\ kHz$ to $144\ kHz$. Frequency sweeping is caused by nonlinear growth of the mode amplitude for a marginally unstable mode with a growth rate much smaller than the drive or damping rate [12]. Weaker modes are also observed at $t = 7.50\ s$ and $f \approx 170\ kHz$.

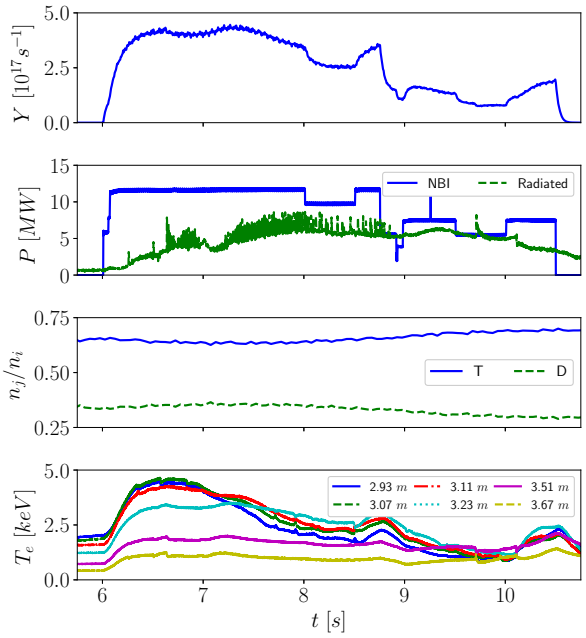

Figure 1: The time evolution of the fusion yield Y; power P of NBI and radiation; the concentrations of ions $j = D, T$ relative to the ion density n_i; and the electron temperature T_e calculated at various major radii.

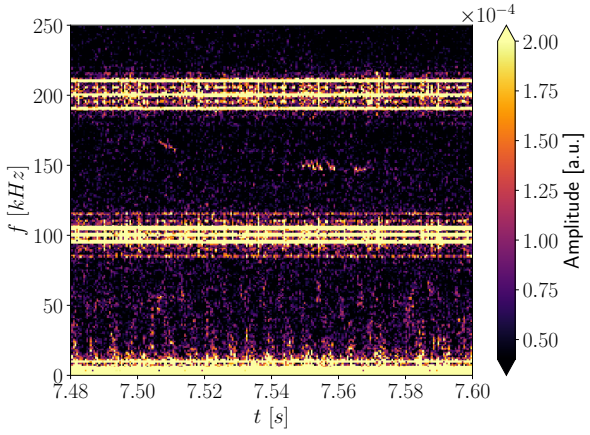

Figure 2: Spectrograph of the perturbed density measured by the fast far-infrared interferometer. The horizontal lines around $f = 0, 100, 200\ kHz$ are artefacts from the diagnostic.

The modes were also observed using an X-mode correlation reflectometer [13], as Figure 3 demonstrates. The probing beam of the reflectometer was programmed to sweep down in frequency [14] and hence cut-off location with a period of 0.6 s, allowing the reflectometer to probe the perturbed density at different radial positions $2.7 \lesssim R(m) \lesssim 3.7$. Therefore, any observed modes can be radially localised within error bars of $\pm 0.1\ m$. The signal is an amalgamation of information about the time of mode excitation and the position of the excited mode. A clear signal was observed at $135 \lesssim f(kHz) \lesssim 170$ at a major radius $3.0 \lesssim R(m) \lesssim 3.4$, allowing for error in the radial localisation of the cut-off position.

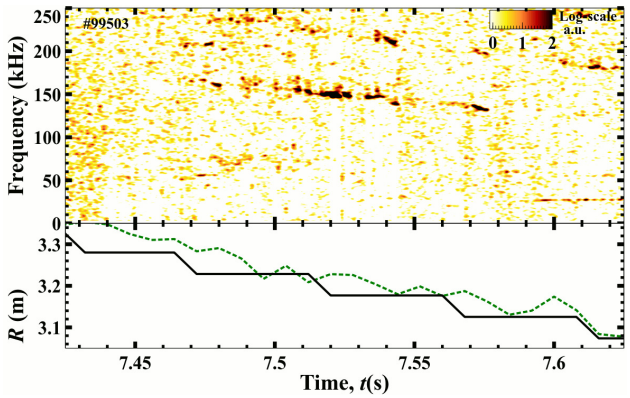

Figure 3: The spectrograph of the reflectometer signal (top), which depends on the radial localisation of the reflectometer cut-off position calculated using two different estimates of plasma density to calculate the cut-off position (bottom).

There were also distinct signals at higher frequencies, but these were not observed in other diagnostics so were not investigated further.

The modes were not observed on magnetic pick-up coils located at the plasma edge. The magnetic coils are more sensitive to modes located near the plasma edge, which undergo less screening by the plasma. The reflectometer indicates that the observed modes were located deep in the plasma so the perturbed magnetic field was likely to be screened by the plasma. Additionally, the modes were relatively weak signals, which may decay to unobservable levels near the magnetic coils. The lack of data from multiple magnetic coils makes it impossible to determine the toroidal mode numbers of the modes. This makes it considerably harder to identify the mode as we must now consider all likely toroidal mode numbers.

3 Modelling

The equilibrium for shot #99503 at time $t = 7.55\ s$ was reconstructed using the equilibrium code EFIT [15]. The safety factor, shown in Figure 4, increases monotonically from $q = 1.6$ on the magnetic axis. The accuracy of the equilibrium reconstruction was improved using pressure and polarimetry constraints. No low-frequency MHD activity was present at $t = 7.55\ s$, but a weak tearing mode was observed from $8.0\ s$ on several toroidally-separated magnetic coils, enabling the identification of the $m/n = 2/1$ tearing mode. The frequency of this tearing mode, $f_{2/1} = 5.2\ kHz$, can be used to determine the location of $q = 2$ flux surface using the monotonically decreasing rotation frequency profile obtained from charge exchange measurements: $f_{2/1} = nf_{rot}(q = 2)$. This method suggests the mode was located at a major radius $R \approx 3.5\ m$. Additionally, a $3/2$ tearing mode excited at $f_{3/2} = 8.4\ kHz$ from $8.48 \leq t(s) \leq 8.58$ was strong enough to appear on the electron cyclotron emission (ECE) diagnostics, enabling the marker to be accurately located from the position of the ECE line of sight: $R \approx 3.2\ m$. Both MHD markers [16] corroborate the accuracy of the q profiles reconstructed with EFIT for this pulse.

Density and temperature profiles are used to compute the collision operators in the LOCUST code. These profiles were calculated using the plasma transport code, TRANSP [17]. The profile reconstruction with TRANSP used electron density measurements from the Thompson scattering and LIDAR diagnostics, electron temperature measurements from Thompson scattering and core ECE diagnostics, and ion

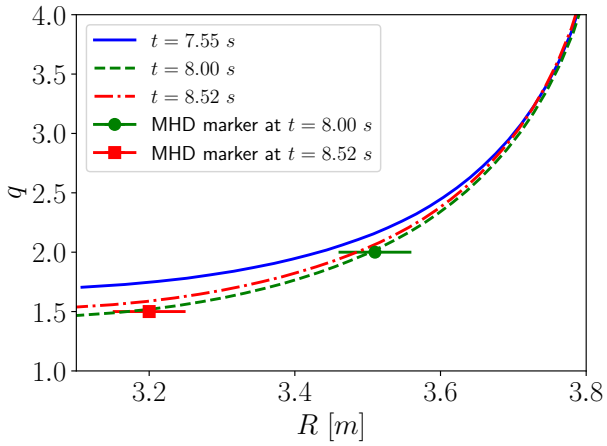

Figure 4: The safety factor q calculated by EFIT as a function of major radius R. Two MHD markers observed later in the pulse are depicted by scatter-points with error bars $\Delta R = 5\ cm$.

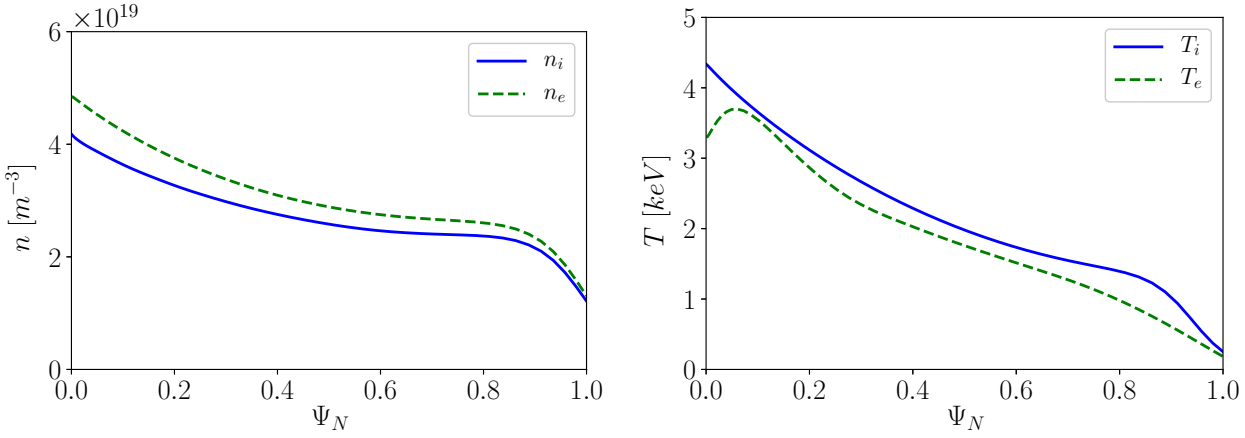

Figure 5: Thermal ion and electron density n and temperature T as a function of normalised poloidal flux Ψ_N reconstructed by TRANSP.

temperature and plasma rotation measurements from charge exchange diagnostics. The resultant density and temperature profiles for $t = 7.55\ s$ are shown in Figure 5. The hollow electron temperature profile is clearly visible, as anticipated from the time traces shown in Figure 1.

3.1 Mode identification

The HELENA code [18] was used to convert the EFIT equilibrium into the straight field line coordinates used by the linear MHD codes, CSCAS [19] and MISHKA-1 [20], which solve the ideal, incompressible MHD equations. The shear Alfvén wave continuum was calculated using CSCAS for toroidal mode numbers $0 \leq n \leq 14$, which is plotted for $n = 9$ in Figure 6. For each continuum, we identify the upper and lower frequency limits of the TAE gap. MISHKA was then used to obtain all eigenmodes present for each toroidal mode number using 20 poloidal harmonics, scanning the initial guess for the eigenfrequency from the lower edge of the TAP gap to the top of the gap over 30 steps. The scanning

script automatically saves unique converged solutions, which were filtered to remove continuum modes. The local toroidal rotation frequency at the location of each candidate mode was added to the plasma frequency of each mode to obtain the mode frequency in the laboratory frame: $f_{lab} = f_{plasma} + nf_{rot}$. We found 80 TAEs that were present in the plasma with toroidal mode numbers $1 \leq n \leq 14$, 25 of which exist in the right approximate location $0 \leq s \leq 0.55$ or $2.9 \leq R(m) \leq 3.4$. Figure 7 shows 21 modes with frequencies $120 \leq f(kHz) \leq 180$ that were selected for stability analysis.

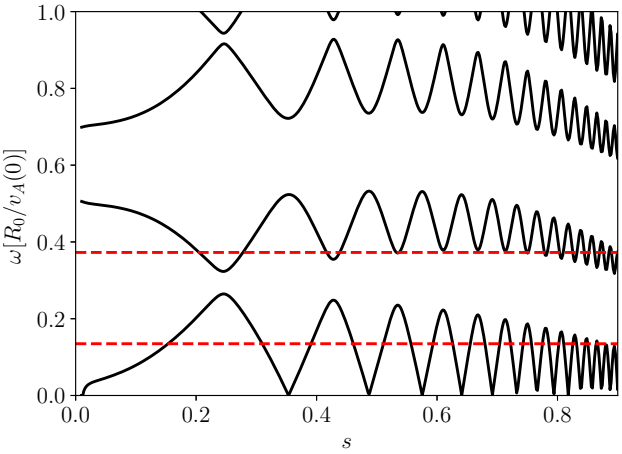

Figure 6: The shear Alfvén wave continuum for the toroidal mode number $n = 9$ showing the frequency ω as a function of the square root of the normalised poloidal flux, $s = \sqrt{\Psi_N}$. The frequency is normalised to the major radius of the magnetic axis R_0 over the Alfvén velocity on the magnetic axis $v_A(0)$. The red dashed lines denote the frequency limits used for the MISHKA-1 scan.

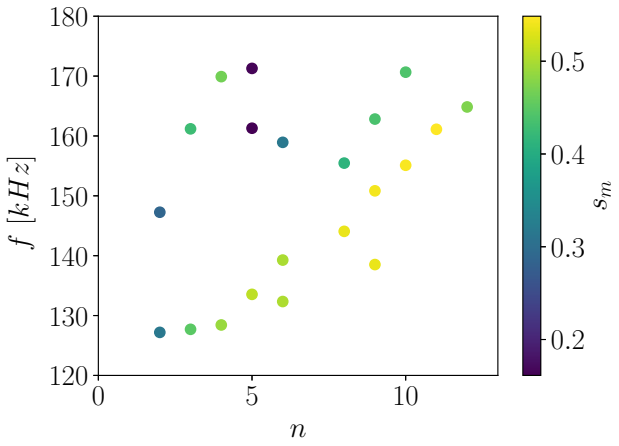

Figure 7: Toroidal Alfvén eigenmodes with toroidal mode number n, frequency f and mode location s_m found using the MISHKA code that match the experimentally observed mode.

3.2 Modelling the beam ion distribution function

We calculated the fast particle distribution functions using the LOCUST code [21]. LOCUST follows the full orbit of a sample of fast ions from birth to thermalisation by solving the Lorentz equation of motion and applying a collision operator. This computationally intensive process is made possible by

exploiting the latest GPU hardware. A LOCUST full orbit simulation of 6M beam ions spanning 0.5 s of plasma time with a time-step of 2 ns takes 25 hours using four NVIDIA A100 GPU cards. A TRANSP-NUBEAM guiding centre simulation of 0.6M particles for the same time-slice ran for eight hours on 32 cores.

The distribution function was calculated by cumulatively binning the fast ion markers on the CPU every 100 ns. This process results in the calculation of the steady-state distribution function through sum reduction by using the entire history of one set of markers from birth until thermalisation or loss from the plasma [22].

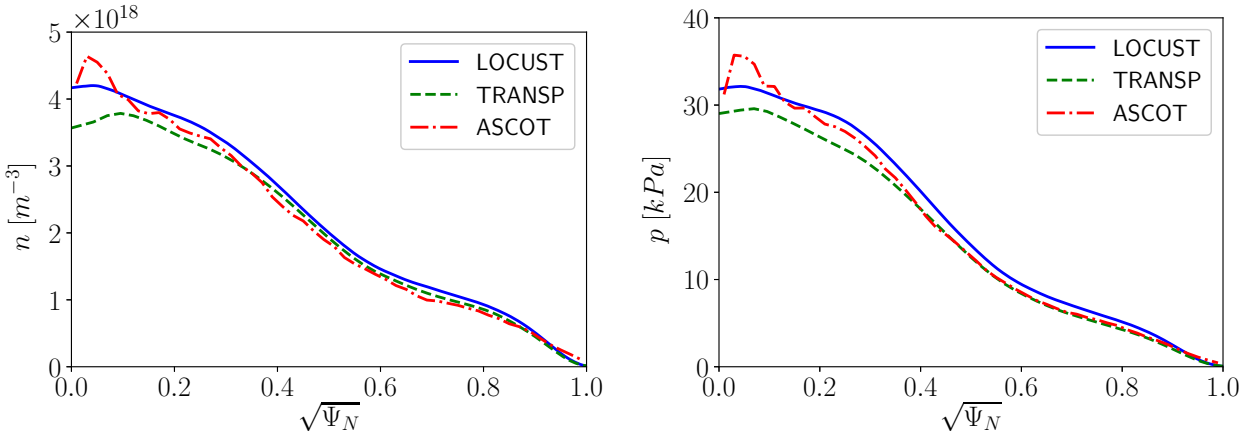

Figure 8: The beam density n and pressure p calculated by LOCUST, ASCOT and TRANSP as a function of the square root of normalised poloidal flux Ψ_N.

LOCUST simulations use ion and electron temperature and density profiles from TRANSP, a 3D tetrahedral wall mesh, a `G EQDSK` file describing the equilibrium calculated by EFIT, and a representative sample of markers to follow. The initial sample of beam ions was generated from the beam deposition in TRANSP-NUBEAM [23]. These markers were then followed until thermalisation, or until the particle terminates on a wall tile. Just 0.5 % of beam ions were lost to plasma-facing components. The moments of the distribution function calculated by LOCUST are shown in Figure 8. The result from LOCUST agrees closely with comparable results from two other codes (TRANSP and ASCOT [24]) for both the beam density and pressure. The moments produced by LOCUST are smoother than the results from TRANSP and ASCOT due to the high number of markers used in the simulation. The ASCOT run used 20K markers, while the TRANSP calculation used 620K markers.

The co-current beam distribution function calculated by LOCUST is depicted in Figure 9 for various values of the magnetic moment. The distribution function is smooth, which is essential for stability calculations. The effect of full, half, and third energy injection is preserved and is visible in the top right and bottom frames of Figure 9. The trapped-passing boundary is visible for sufficiently high μ. The left edge in each frame is a result of the condition $\mu B \leq E$, with the angle determined by $B(R)$. The lower edge in each frame corresponds to the magnetic axis, with the angle determined by the first term in the toroidal canonical angular momentum $\sim m_j R v_\phi$. These features are typically lost when using analytical expressions or fits of Monte Carlo-generated distribution functions.

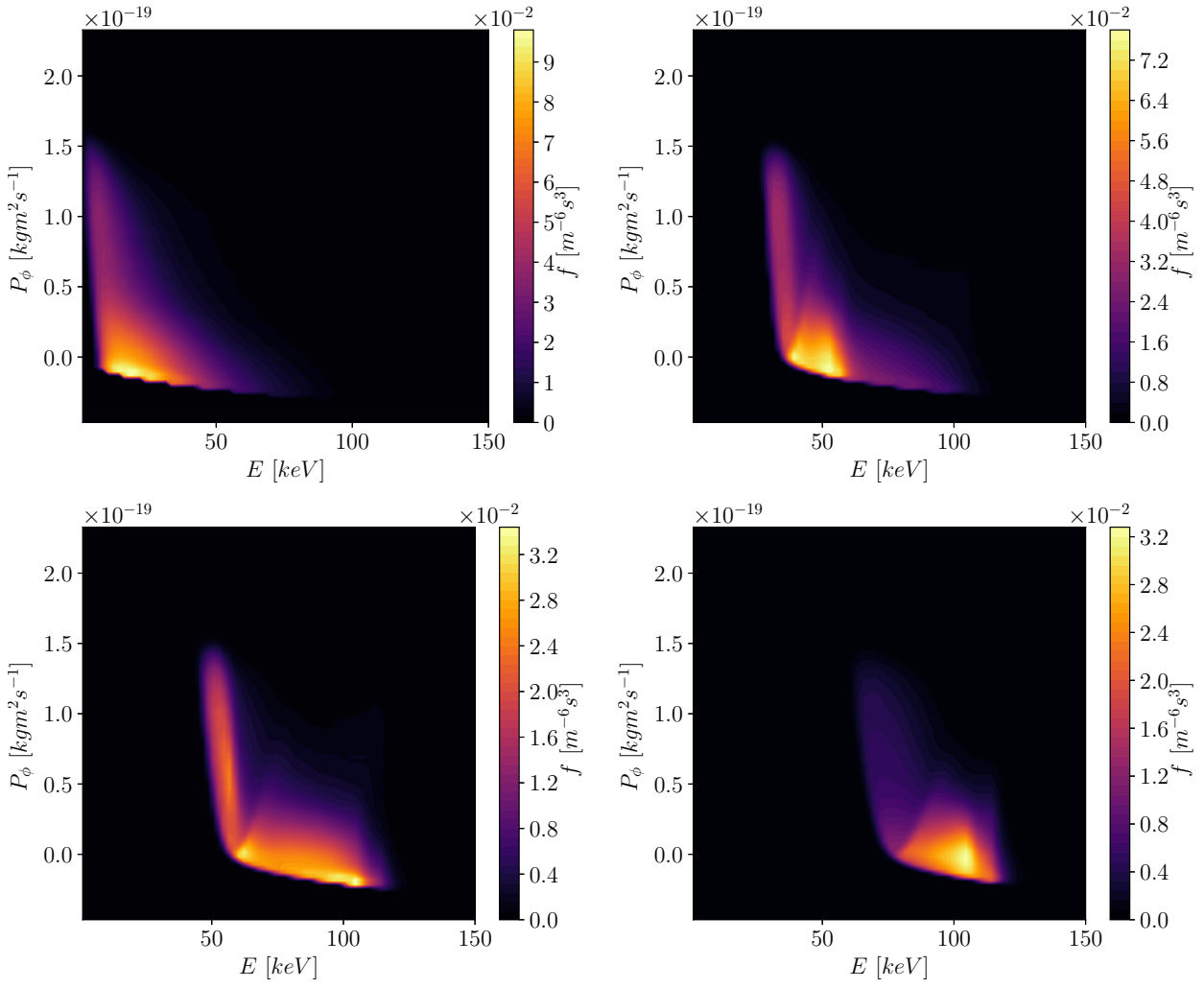

Figure 9: The $\sigma = +1$ beam distribution function f as a function of energy E and toroidal canonical angular momentum P_ϕ for fixed values of the magnetic moment: $\mu = 1.1keV/T$ (top left), $\mu = 9.6keV/T$ (top right), $\mu = 15.2keV/T$ (bottom left), $\mu = 20.2keV/T$ (bottom right).

3.3 Modelling the alpha particle distribution function

TRANSP simulations show that beam-thermal fusion reactions dominate over thermonuclear and beam-beam reactions for our shot, with 97% of alpha particles produced in beam-thermal reactions. We generate alpha particles born in beam-thermal fusion by using the beam distribution function computed by LOCUST to generate a set of representative beam ions. A set of thermal particles at the same locations as the beam particles was produced from a Maxwellian distribution. The reaction rate for an alpha particle produced in a fusion reaction between each thermal and beam particle was calculated with Bosch-Hale [25] cross-sections and used as the alpha particle weight in LOCUST. The velocity of the alpha particles was determined through the application of kinematic principles to the velocities of the reactants [26].

This sample of alpha particles was then loaded in LOCUST and followed until thermalisation. The

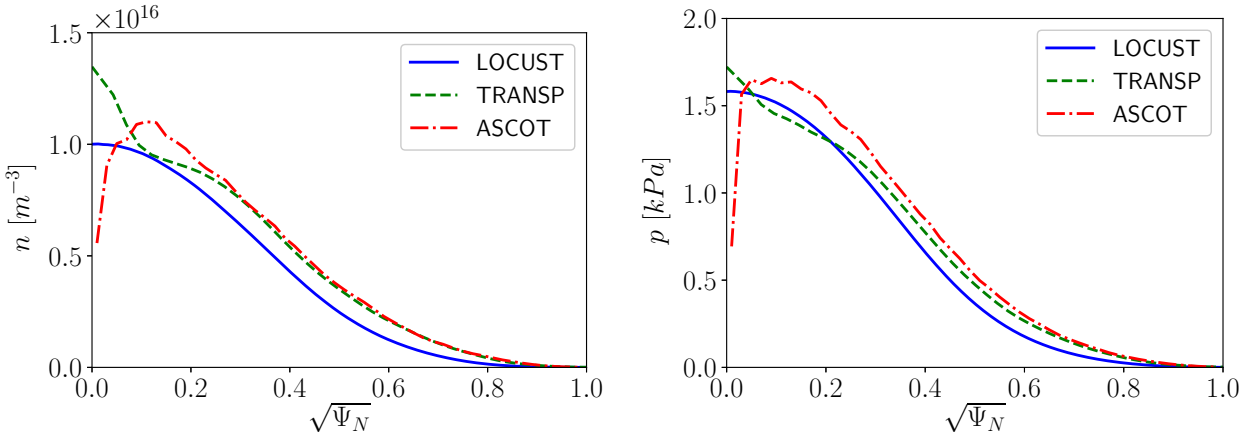

Figure 10: Alpha particle density n and pressure p calculated by LOCUST, ASCOT and TRANSP as a function of the square root of normalised poloidal flux Ψ_N.

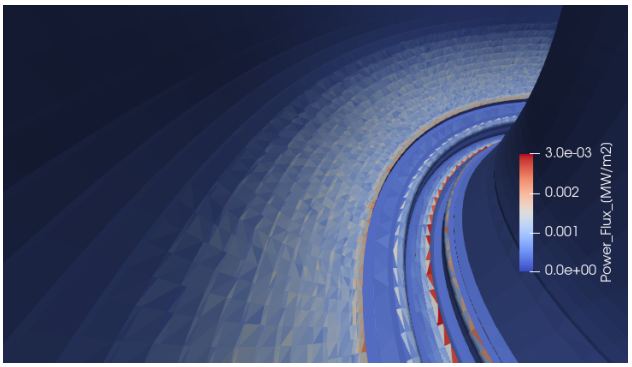

Figure 11: The power flux on the first wall due to losses of beam-thermal fusion born alpha particles calculated by LOCUST looking down at the divertor from the midplane.

moments of the resultant alpha particle distribution function calculated by LOCUST are shown in Figure 10. The density and pressure profiles from LOCUST largely agree with the results from TRANSP and ASCOT. However, the alpha particle density and pressure calculated by LOCUST are slightly lower than the profiles from TRANSP and ASCOT. This difference is attributed to a higher loss rate of alpha particles calculated by LOCUST, which follows the full gyro-orbit, compared to TRANSP and ASCOT, which follow the particle guiding centres in these simulations. The size of the alpha particle orbits is relatively large compared to the minor radius of the plasma. Therefore, a large portion of the fusion-born alpha particles was lost to the plasma-facing components. For $t = 7.55\ s$, 19 % of alpha particles were lost. 95 % of these losses were prompt losses, with collisional scattering onto lost trajectories making up the other 5 % of losses in our axisymmetric equilibrium. The lost alpha particles cause a peak power flux to the first wall of $3\ kW/m^2$, as shown in Figure 11, which is well within the tolerances of the wall. The top corners of tiles 1 and 5 receive the highest power fluxes. The losses drop off towards the mid-plane of the tokamak. This loss rate is consistent with losses of fusion-born alpha particles in other JET DT pulses that have been modelled. For example, for the afterglow experiment [6], LOCUST finds rates of 19 % for alpha particles produced in D beam-thermal reactions were lost, 20 % for alpha particles produced in T beam-thermal reactions, 15 % of beam-beam fusion-born alpha particles and 26 % of

thermonuclear alpha particles. The difference between each population of alpha particles is attributed to the profiles of the reactants — the beam ion density profile is more peaked than the thermal ion density profile.

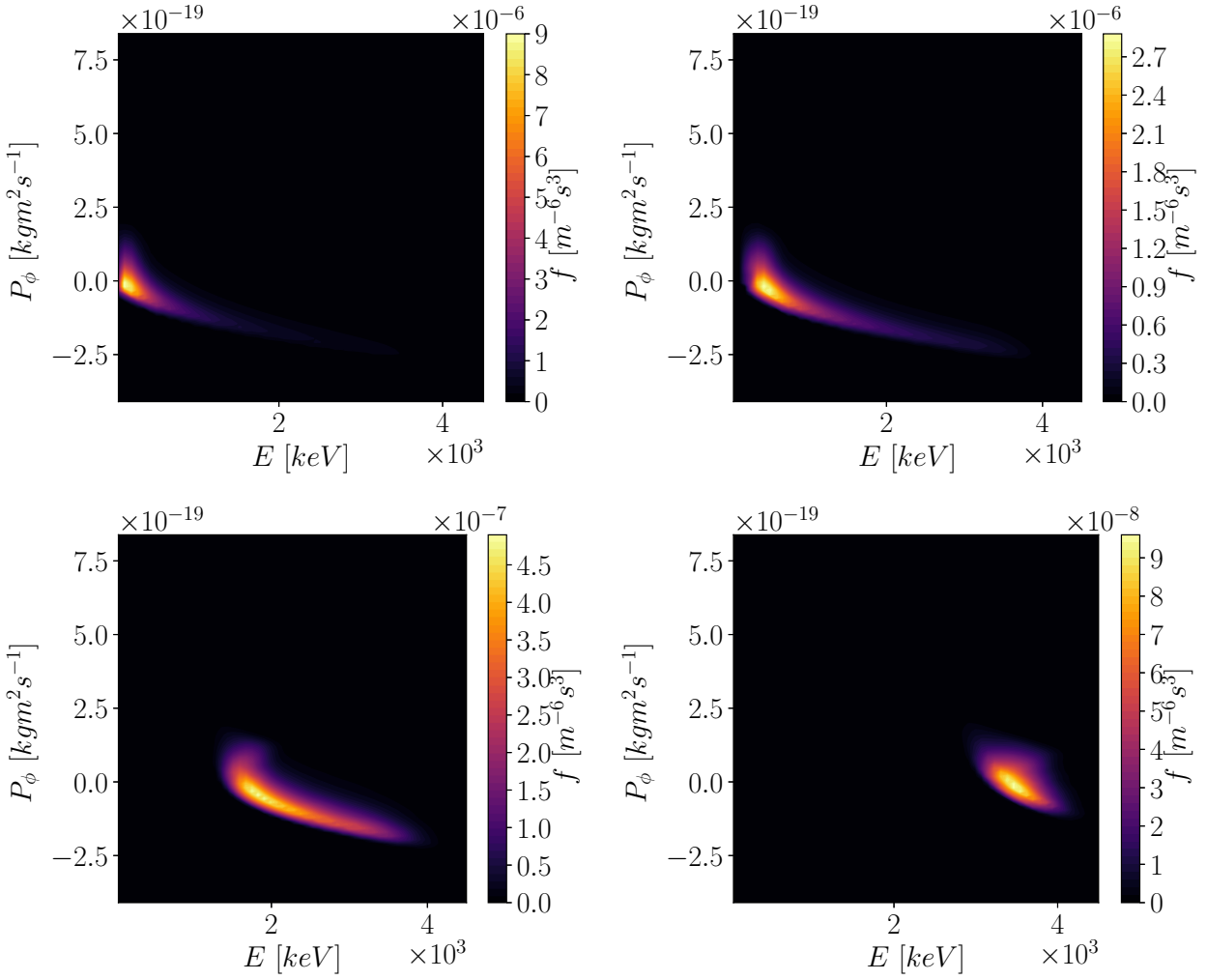

Figure 12: The $\sigma = +1$ alpha particle distribution function f as a function of energy E and toroidal canonical angular momentum P_ϕ for fixed values of the magnetic moment: $\mu = 43.1keV/T$ (top left), $\mu = 100.5keV/T$ (top right), $\mu = 416.5keV/T$ (bottom left), $\mu = 904.8keV/T$ (bottom right).

The alpha particle distribution function is plotted at constant μ in Figure 12 for the co-current direction. In general, the alpha particle distribution function is considerably simpler than the beam distribution function. The alpha particle distribution function is strongly peaked around the magnetic axis due to the more narrow birth profile. The distribution function is more peaked in E and P_ϕ at lower μ because the alpha particle orbit width increases significantly with $v_\perp$. The trapped-passing boundary is not as distinct as in the beam distribution function.

3.4 Modelling the interaction of TAEs with fast particles

The eigenstructure of each candidate mode from MISHKA and the fast particle distribution functions were used as input for the perturbative code HALO [27], which uses a δF scheme [28]. The distribution functions produced by LOCUST require light processing before use in HALO. First, the distribution function must be reshaped to the order used by HALO. Second, singularities present in the $\sigma = -1$ distribution function due to zeroes in the Jacobian were removed using a median filter that replaces each singular point with the local median using three neighbouring points in each dimension. Finally, the distribution function is processed using a Chambolle total variation algorithm [29]. The Chambolle smoothing algorithm removes excess noise by minimising the total variation of the distribution function. The growth rate calculated by HALO is insensitive to the total variation process, which will be demonstrated later in the paper.

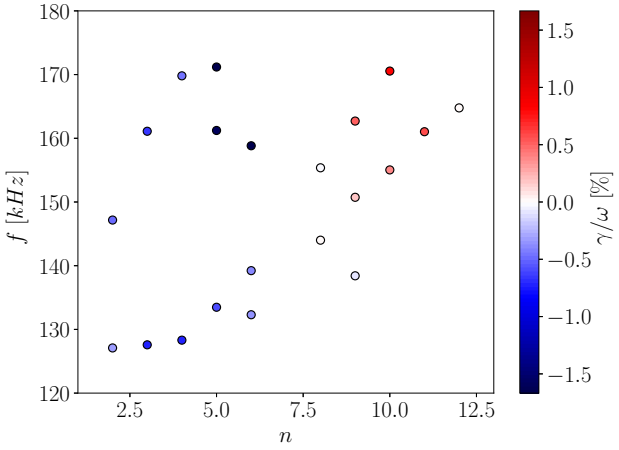

Figure 13: Linear growth rates γ normalised to the wave frequency ω due to the interaction of beam ions with 21 TAEs with toroidal mode numbers n and lab frame frequencies f.

Full gyro-orbit calculations of linear wave-particle interactions were carried out using the distribution functions calculated with LOCUST and the TAEs found using MISHKA. The stability of each mode shown in Figure 7 was calculated over eight wave periods, this simulation time was chosen for a reliable, converged growth rate that minimises the use of computational resources. 4M particles were followed with a time-step of $10^{-10}\ s$. The power transfer with each TAE, which started with initial mode amplitudes $\delta B_r/B_0 = 10^{-7}$, was measured to assess the growth rate of each mode. The stability calculation for each mode required 1.5 hours of computational time using four A100 GPU cards. The resultant linear growth rates due to interaction with the beam ions are shown in Figure 13. The population of beam ions damp modes with toroidal mode numbers $n < 8$ with damping rates $-\gamma/\omega \lesssim 1.6\%$. However, modes with toroidal mode numbers $n \geq 8$ are driven by P_ϕ gradients in the fast particle distribution function. The mode width is greater than the average orbit width of resonant ions for $n \geq 8$, qualitatively agreeing with the parametric study of Seo and colleagues [9]. The drive peaks at $n = 10$ at $\gamma/\omega = 1.0\%$ and begins to slowly decrease for $n \gtrsim 10$ as particle orbits become large relative to the mode width $\sim r_m/nq$.

Drive of TAEs by beam ions is unexpected — beam ions are usually assumed to damp TAEs in JET [8, 9]. However, an analytical calculation of the ion diamagnetic frequency ω_*/ω for the same modes reveals the same qualitative picture: high n TAEs can be driven by radial gradients of the beam pressure, as shown by Figure 14. This is unsurprising when one considers the first term of Equation 1, which shows

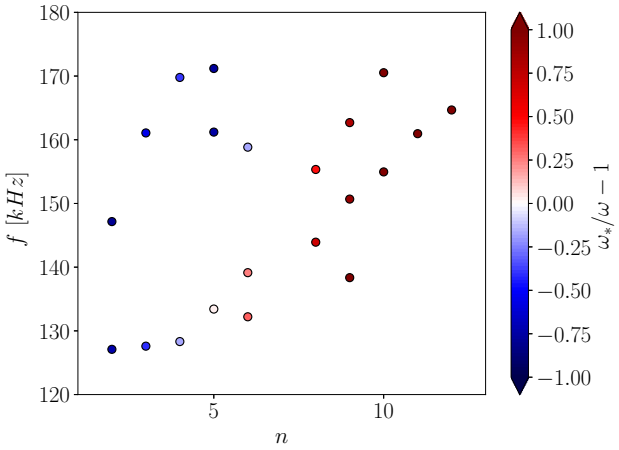

Figure 14: The ion diamagnetic frequency ω_* divided by the wave frequency ω for 21 TAEs with toroidal mode numbers n and lab frame frequencies f. Blue represents damping of a mode, while red signifies drive.

that the drive rate from P_ϕ gradients is proportional to the toroidal mode number. As the toroidal mode number increases, the drive from radial gradients can overcome the damping from energy gradients of the distribution function.

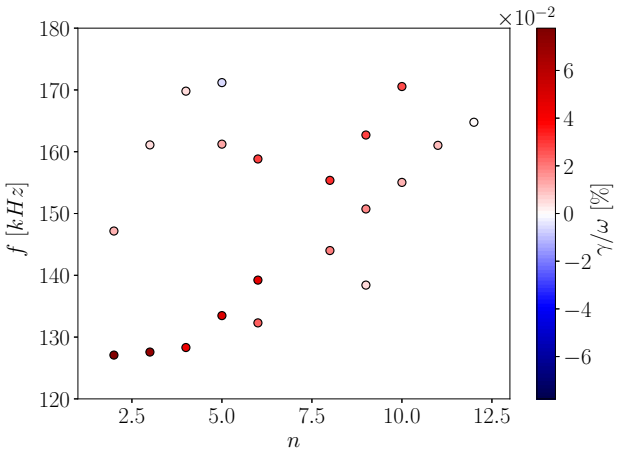

Figure 15: Linear growth rates γ normalised to the wave frequency ω due to the interaction of alpha particles with 21 TAEs with toroidal mode numbers n and lab frame frequencies f.

The growth rate due to the interaction between alpha particles and the candidate modes was computed using the same settings as the beam ion calculation. The resultant linear growth rates are shown in Figure 15. The growth rates due to alpha particles are one or two magnitudes smaller than those of beam ions due to the low alpha power generated in this experiment. All modes except one odd mode were driven by the alpha particle population. The $n = 5$ TAE that is damped by the alpha particles is located deep in the plasma with an anti-ballooning mode structure.

Guiding centre calculations are approximately 100 times faster than gyro-orbit calculations, but the time saved comes at the cost of accuracy. The difference between the growth rate from the guiding centre and gyro-orbit calculations increases with toroidal mode number, as depicted in Figure 16. When the

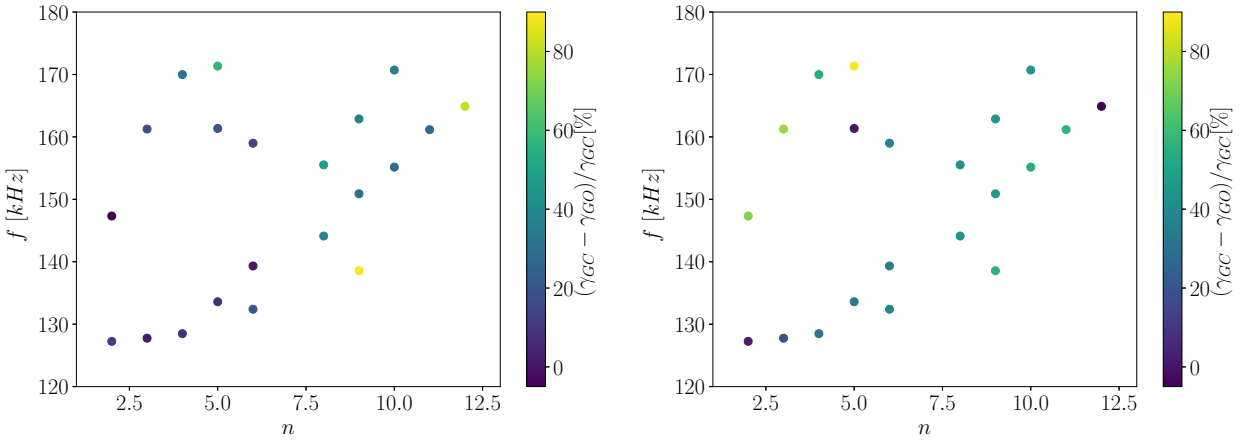

Figure 16: The difference between the guiding centre (GC) and gyro-orbit (GO) calculations of the linear growth rate caused by beam ions (left) and alpha particles (right) for 21 TAEs with toroidal mode numbers n and lab frame frequencies f.

mode width $\sim r_m/m$ is comparable to the ion gyroradius, the drive of the mode reduces due to a weakening of the resonant particle coupling to the mode. Analytical expressions account for this by including an additional factor $J_0(mv_\perp/r_m\omega_c)$ [30] for full orbit calculations of the linear growth rate compared to guiding centre calculations, where J_0 is the zeroth Bessel function of the first kind. While the difference is greater for alpha particle stability calculations, the discrepancy is still significant for beam ions for high toroidal mode numbers $n \gtrsim 8$. The discrepancy between gyro-orbit and guiding centre calculations is more significant at low n for alpha particles than for beam ions because the ratio of the perpendicular velocity to ion cyclotron frequency $v_\perp/\omega_{ci}$ is much larger for highly energetic alpha particles. Modes located at higher major radii were also more strongly affected, due to the lower local magnetic field and therefore larger factor $\sim 1/\omega_{ci}$. Figure 16 underlines the importance of using full gyro-orbit calculations for both beam and alpha particles, particularly for high n marginally unstable modes, or modes in weak magnetic fields.

3.5 Computing damping due to interactions with the bulk plasma

The interaction with fast particles is just one aspect of the mode stability. Non-ideal effects, such as parallel electric fields and finite Larmor radius of thermal particles, couple TAEs with kinetic Alfvén waves (KAWs) [31]. KAWs can travel in the direction perpendicular to the equilibrium magnetic field, carrying energy away from the TAE in the parallel electric field. As the KAW reaches regions with high k_r and thus high dissipation, this energy is transferred to the trapped electron population in a process known as radiative damping. The coupled TAE-KTAE propagates with the dispersion relation [32]:

$$\omega^2 = k_\parallel^2 v_A^2 \left[1 + k_\perp^2 \rho_i^2 \left(\frac{3}{4} + \frac{T_e}{T_i}\left(1 - \mathrm{i}\delta\right)\right)\right], \tag{4}$$

where the thermal ion Larmor radius $\rho_i = \sqrt{m_i T_i}/eB$ and the rate at which the energy of the kinetic Alfvén wave is collisionally dissipated into the trapped electron population:

$$\delta \simeq 0.44\sqrt{\frac{\nu_e}{\omega}}\left(\ln\sqrt{\frac{\varepsilon\omega}{2\nu_e}}\right)^{-\frac{3}{2}}, \tag{5}$$

where ν_e is the electron collision frequency and $\varepsilon \approx \frac{5}{2}\frac{r_m}{R_0}$ is the toroidicity.

Including non-ideal effects in the wave equation produces equations analogous to the resistive MHD equations with a complex resistivity if $|\eta k_r^2/\omega| \ll 1$, where the complex resistivity is defined as [32, 33]:

$$\eta = \mathrm{i}\left(\frac{3}{4} + \frac{T_e}{T_i}(1 - \mathrm{i}\delta)\right)\frac{\omega}{\omega_{A0}}\left(\frac{\omega}{\omega_g}\right)^2\left(\frac{\rho_i}{R_0}\right)^2, \tag{6}$$

where $\omega_g = v_A(R)/2qR$ is the frequency of the TAE gap and $\omega_{A0} = v_A(R_0)/R_0$. The inclusion of complex resistivity in the CASTOR code [32] enables the calculation of the radiative damping rate for a mode. For each mode, the imaginary part of the resistivity was calculated at the mode location and kept fixed while the dissipation rate, and therefore real resistivity, was steadily decreased to zero from 1.0 [33, 34]. For low dissipation rates, the computed damping rate initially increases rapidly with the dissipation rate. Above a critical value of the dissipation rate, the computed damping rate becomes linearly dependent on the dissipation rate of the TAE when all kinetic Alfvén wave energy is dissipated. Extrapolating the gradient above this critical point back to $\delta = 0$ reveals the radiative damping rate. Figure 17 shows the radiative damping rate for the TAEs found with MISHKA. As expected from analytical estimates, the radiative damping rate increases with poloidal mode number m and therefore toroidal mode number n.The damping rate $-\gamma_{rad}/\omega \gtrsim 0.5\%$ for all modes with $n \geq 8$.

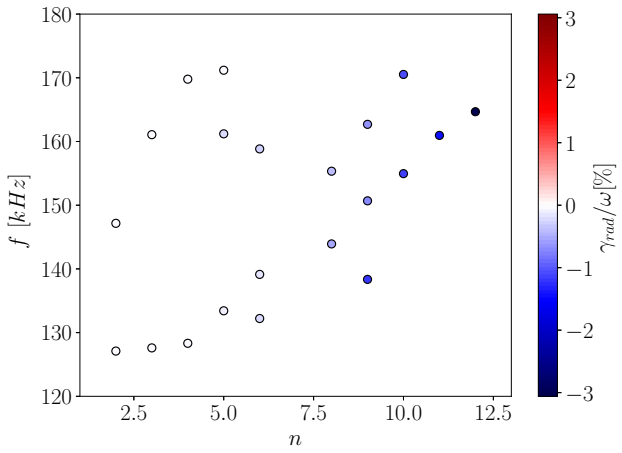

Figure 17: The radiative damping rate γ_{rad} normalised to the wave frequency ω for 21 TAEs with toroidal mode numbers n and lab frame frequencies f.

We can also use CASTOR to calculate the damping rate for trapped electron collisional damping, which occurs due to collisional dissipation of eigenmodes caused by collisions of trapped electrons with ions and passing electrons [35]. The damping rate was computed by using the experimental value of the real resistivity and zero imaginary resistivity [36]. We use this technique to find the collisional damping rate for all candidate modes. Collisional damping is most significant for low-shear even modes, as shown in Figure 18. The collisional damping rate is sensitive to the mode location, with all modes at positions $s_m \leq 0.5$ experiencing damping $\gamma_{coll}/\omega \leq 3.2 \times 10^{-4}$, while all modes in the outer half of the plasma experience significant collisional damping.

Continuum damping occurs when the eigenfrequency matches the frequency of the shear Alfvén continuum and the mode amplitude is significant at the location of the continuum intersection [37]. This leads to a resonant power absorption as the eigenmode is converted into a kinetic Alfvén wave, which propagates across magnetic field lines and dissipates on the higher density side of the plasma. The con-

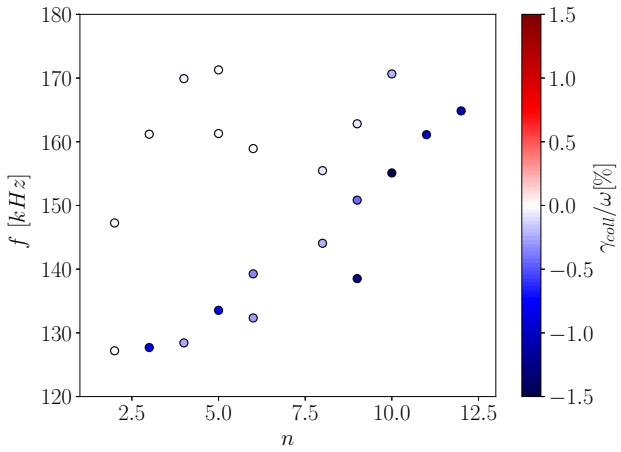

Figure 18: The collisional damping rate γ_{coll} normalised to the wave frequency ω for 21 TAEs with toroidal mode numbers n and lab frame frequencies f.

tinuum damping rate was assessed using CASTOR using real resistivity only. As the real resistivity tends to zero, the imaginary frequency tends to the continuum damping rate [38, 36]. Using this method, we assess the continuum damping rate for all candidate modes, with the results shown in Figure 19. The continuum damping was small for all modes, $2.5 \times 10^{-6} \leq \gamma_{cont}/\omega \leq 1.2 \times 10^{-3}$, due to the small amplitude of the modes at the location at which the eigenfrequency hits the continuum. It was more significant for low n modes due to their wide mode width.

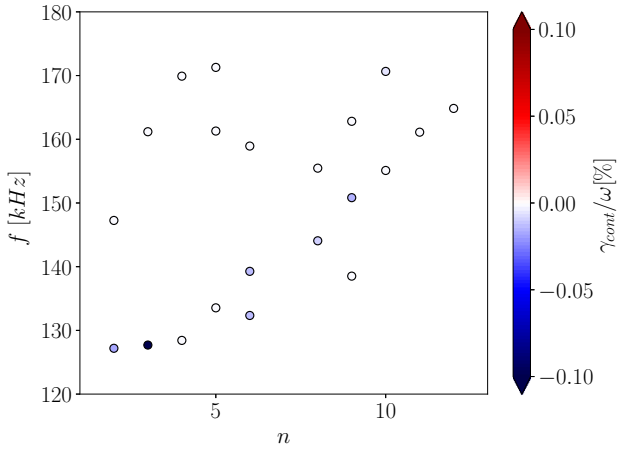

Figure 19: The continuum damping rate γ_{cont} normalised to the wave frequency ω for 21 TAEs with toroidal mode numbers n and lab frame frequencies f.

Finally, we can use HALO to assess the effect of ion Landau damping, which is caused by the resonant transfer of power from the TAE to thermal ions through relatively inefficient side-band resonances $\sim v_A/v_{Th}/(2j+1)$ where $j \gg 0$. The power transfer can be assessed in HALO using an analytical Maxwellian distribution function instead of the LOCUST-generated distribution function. The linear ion Landau damping rates due to interactions between the bulk ions and the candidate modes are shown in Figure 20. The ion Landau damping rates were small for all TAEs, $1 \times 10^{-5} \leq \gamma_D/\omega \leq 5 \times 10^{-4}$ and $3 \times 10^{-7} \leq \gamma_T/\omega \leq 1 \times 10^{-3}$, due to the low plasma temperature and high magnetic field of the plasma, which lowers the thermal velocity and increases the Alfvén velocity, respectively.

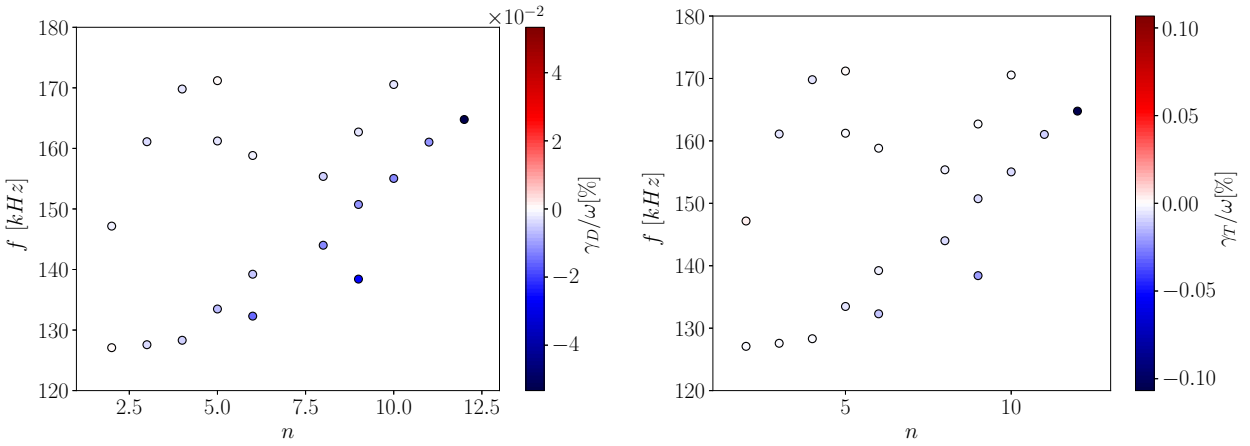

Figure 20: The ion Landau damping rate due to D thermal ions γ_D (left) and T thermal ions γ_T (right) normalised to the wave frequency ω for 21 TAEs with toroidal mode numbers n and lab frame frequencies f.

In summary, high n even modes were heavily radiatively damped, low-shear even modes were collisionally damped, while all low n modes were heavily damped by beam ions. Comparing the result with the total growth rate due to beam and alpha particles, we find one mode that is marginally unstable, as shown in Figure 21. The net-driven mode with toroidal mode number $n = 9$, lab frequency 163 kHz and location $s_{max} = 0.44$ ($R_{max} = 3.31\ m$) has an even mode structure, as shown in Figure 22, with dominant poloidal harmonics $m = -16$ and $m = -17$ and significant contributions from higher poloidal harmonics. The computed growth rates for the net-driven $n = 9$ mode are shown in Table 1, producing net drive of $\gamma_{net}/\omega = +0.02\%$. While the drive from alpha particles is small, it plays a key role in pushing the mode to instability. These calculations are corroborated by the observation of chirping behaviour, a nonlinear phenomenon that occurs near the stability threshold.

γ_b/ω	γ_α/ω	γ_{rad}/ω	γ_{coll}/ω	γ_{cont}/ω	γ_D/ω	γ_T/ω
6.9×10^{-3}	2.8×10^{-4}	-6.0×10^{-3}	-6.7×10^{-4}	-1.5×10^{-5}	-2.7×10^{-5}	-1.0×10^{-5}

Table 1: A table showing the drive and damping rates for the $n = 9$ net-driven TAE with frequency $f = 163\ kHz$.

The power transfer from each beam ion marker to the $n = 9$ mode is shown in Figure 23. The largest contribution to the mode stability comes from the $p = 4$ ($v_\parallel = v_A/5$) resonance. The $p = 4$ resonance damps the TAE for $\mathcal{E} \geq 105keV$ because the full-energy injection creates steep, negative energy gradients, which can be seen in the full beam distribution function in Figure 9. A simpler picture of the distribution function is shown in Figure 24, where P_ϕ and μ have been integrated over. These energy gradients reduce ω_* so that $\omega_* < \omega$ and the wave is damped. For $60 \leq \mathcal{E}(keV) \leq 105$ the energy gradients are gentle, ω_* is large, and the mode is driven. At $\mathcal{E} \approx 60keV$, the half-energy beam injection again produces strong negative energy gradients, damping the TAE. For $\mathcal{E} < 50keV$, particles weakly drive the TAE. A similar effect is observed for weaker (but still significant) resonances $p = 3$, 2 and 1.

For modes with toroidal mode numbers $n < 8$, the net damping arising from the full energy injection at $\mathcal{E} \geq 105keV$ dominates over drive from $\mathcal{E} < 105keV$. The $p = 4$ resonance still dominates the

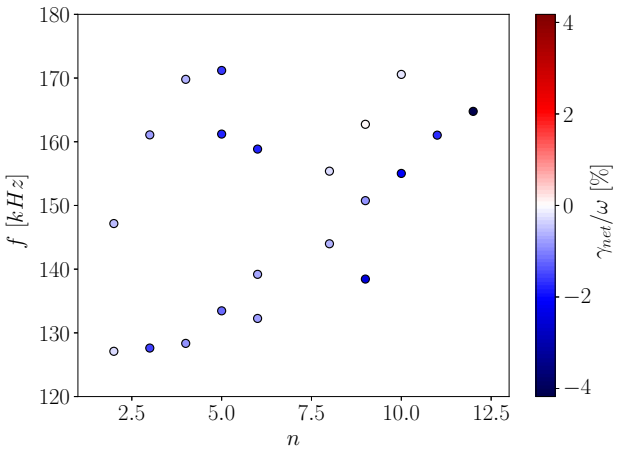

Figure 21: The net growth rate γ_{net} normalised to the wave frequency ω for 21 TAEs with toroidal mode numbers n and lab frame frequencies f.

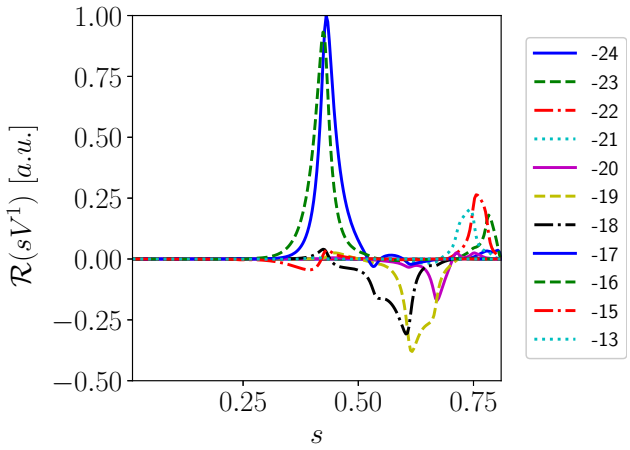

Figure 22: The wave potential $\mathcal{R}(sV^1)$ as a function of the square root of normalised poloidal flux $s = \sqrt{\Psi_N}$ for the net driven $n = 9$ TAE. Different line colours and styles depict significant poloidal harmonics.

mode stability calculation for low n. For modes with higher drive than the $n = 9$ mode of interest, the damping contribution from $\mathcal{E} \geq 105keV$ is weaker than the drive from lower energies along the $p = 4$ resonance.

The power transfer is dominated by interactions between the dominant poloidal harmonics $m = -16$ and -17 and particles located at the wave maximum at a major radius $R \approx 3.3\ m$, as shown on the left-hand side of Figure 25. A typical orbit of a resonant ion overlaid over the wave field is shown on the right-hand side of Figure 25. 70% of the net power transfer comes from 0.08% of the particles. Of these highly resonant particles, 3% were trapped particles, 12% were counter-passing and 85% were co-passing ions. Almost all of the resonant counter-passing particles damp the mode.

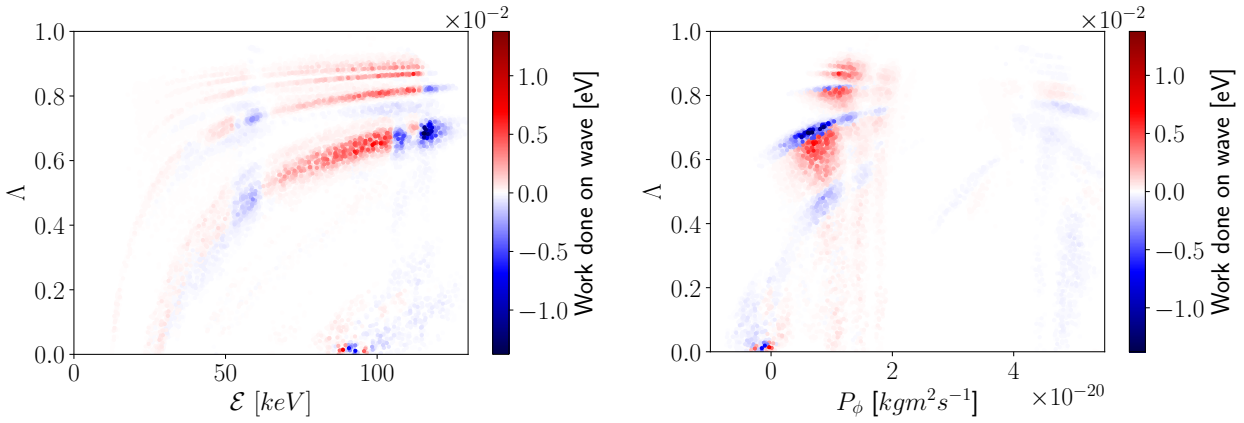

Figure 23: The work done on the $n = 9$ TAE of interest by the highly resonant beam ions in HALO as a function of energy $\mathcal{E}$, the pitch invariant $\Lambda = \mu B_0/\mathcal{E}$ and the canonical toroidal angular momentum P_ϕ. Red denotes drive and blue denotes damping of the TAE.

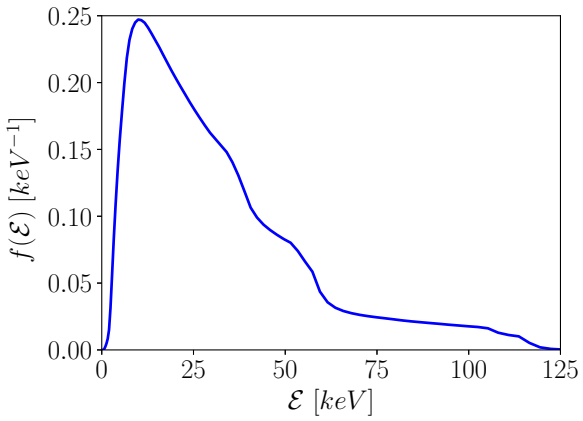

Figure 24: The beam ion energy $\mathcal{E}$ distribution function $f(\mathcal{E})$ integrated over the magnetic moment and canonical toroidal angular momentum.

4 Discussion

Beam-driven TAEs have not been identified in JET before. The absence of ICRH-accelerated ions in this experiment allows for a more accurate determination of the source of the mode drive. The high magnetic field used in our experiment reduces non-ideal damping effects $\sim k_\perp \rho_i$. Additionally, the electron temperature was low due to the relatively low beam power, resulting in reduced radiative damping.

The unique characteristics of our experiment are summarised in Figure 26. The data points at high T_e and low beam power are pulses with high ICRH power. Shots from our experiment, known as the bump-on-tail (BOT) experiment, have higher $q(0)^2$ than shots with similarly low beam power and electron temperature, enhancing the drive from beam ions and alpha particles, which scales as $\sim q^2$. Increasing beam power further increases the electron temperature and therefore damping. The effect of the low electron temperature on radiative damping was explored by scanning the electron temperature used in

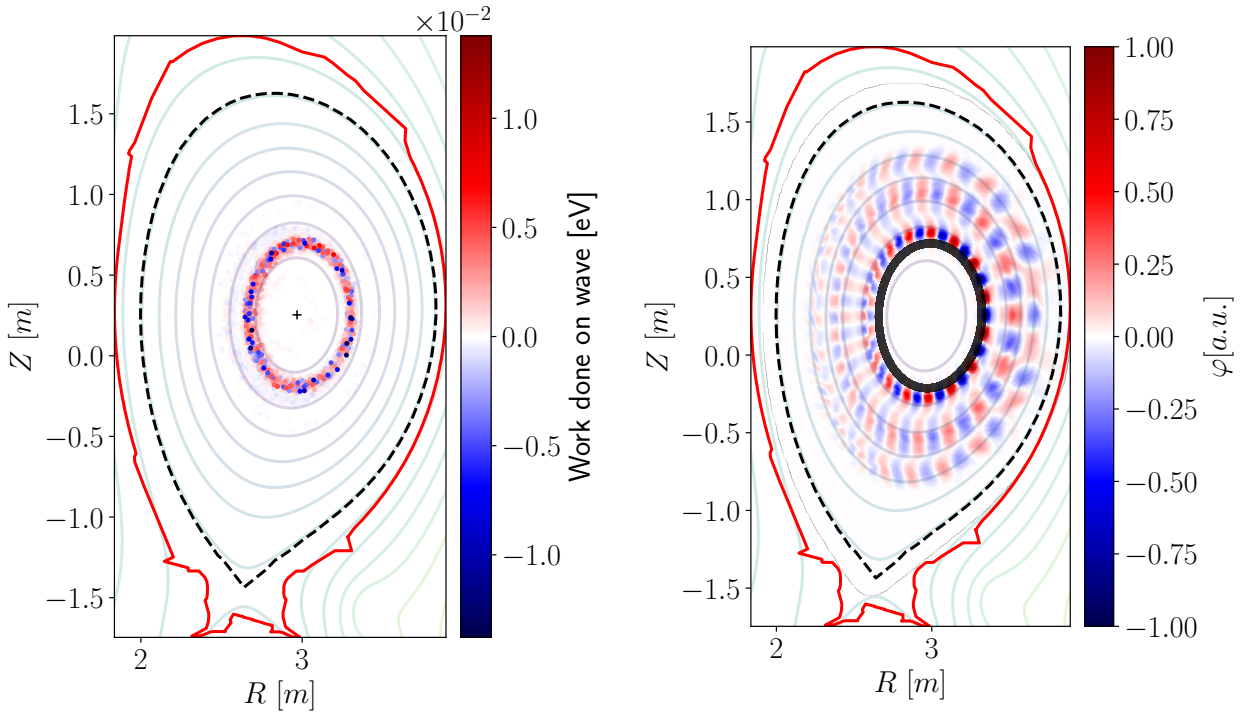

Figure 25: Left: the work done on the net-driven $n = 9$ TAE by markers in HALO as a function of major radius R and height Z, where red denotes drive and blue denotes damping of the TAE. Right: a typical orbit of a highly resonant ion superimposed on the structure of the wave field, where colour represents the electrostatic potential. In both figures flux contours are shown in the background, a dashed black line denotes the last closed flux surface and the first wall is shown by a solid red line.

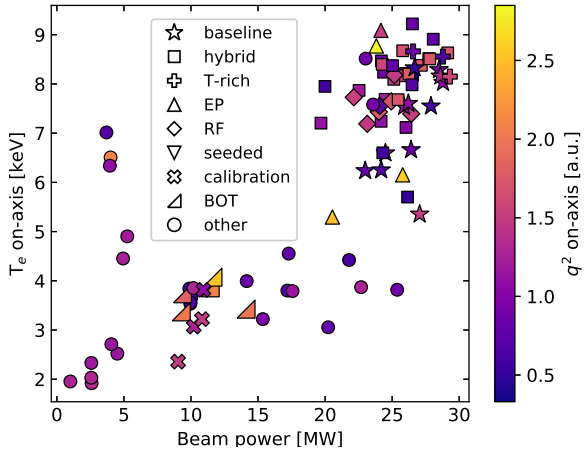

Figure 26: Electron temperature T_e on the magnetic axis against beam power, with the colour representing the safety factor on-axis for all validated TRANSP simulations spanning the DT campaign. Our shots are labelled as 'BOT', and the other experiments are described in Ref. [39].

CASTOR. Figure 27 shows that the radiative damping rate increases approximately linearly with electron

temperature. Given that the $n = 9$ mode was only marginally unstable, a modest increase in radiative damping would be sufficient to suppress the mode.

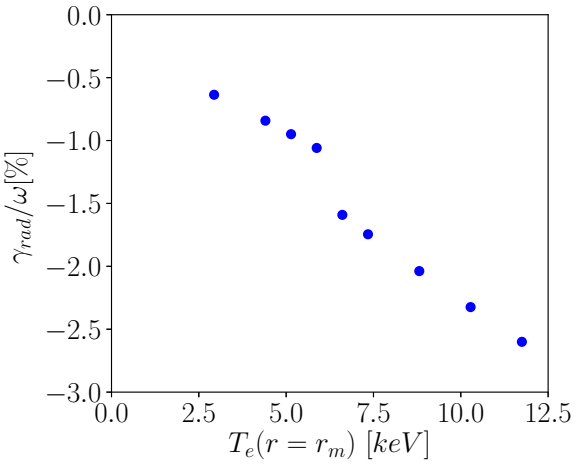

Figure 27: The dependence of the radiative damping rate γ_{rad} normalised the wave frequency ω calculated by CASTOR on the electron temperature T_e at the mode position r_m.

4.1 Numerical convergence of the linear growth rate

A sufficiently large number of markers must be followed in LOCUST to ensure the critical features of the distribution function are properly resolved. Figure 28 shows the dependence of the growth rate on the number of beam ions loaded in LOCUST, N_L. For each point, a distribution function was generated using N_L markers in LOCUST. This distribution function was then used in HALO, which loaded $N_H \approx 4M$ markers for each run. $N_L \gtrsim 6M$ markers must be used to resolve all key features of the beam distribution function in LOCUST, for example, the trapped-passing boundary and full, half and third energy beam injection. For $N_L \lesssim 6M$, the growth rate steadily decreases with N_L. The growth rate fluctuates if $N_L \lesssim 1M$ markers are used. The alpha particle distribution function is less sensitive to the number of markers used. Running LOCUST with $N_L \sim 1M$ alpha particles is sufficient to capture all of the key features of the alpha particle distribution function. The alpha particle distribution (Figure 12) is considerably less detailed than the beam distribution function (Figure 9).

Similarly, it is important to load a sufficient number of markers into HALO N_H. The distribution function calculated with $N_L = 6M$ LOCUST markers was used for a series of HALO runs using varying numbers of HALO markers. Figure 29 shows that $N_H > 4M$ markers in HALO is required to obtain a converged linear growth rate when using the full distribution function generated by a Monte Carlo code. For $N_H \lesssim 2M$ markers, the linear growth rate drops off to $\sim 1/3$ of the converged value, and it begins to rapidly vary for $N_H \lesssim 131K$ markers. Figure 30 shows the corresponding scan for alpha particles. The number of HALO markers required for a converged growth rate is significantly lower for alpha particles than for beam ions. Just $N_H \sim 131K$ is sufficient to obtain the linear growth rate to within 10% of the converged value.

Finally, we check the dependence of the linear growth rate of the $n = 9$ TAE on the Chambolle total variation algorithm, which was used in the pre-processing of the distribution function. Figure 31 shows very little variation in the linear growth rate over seven orders of magnitude of the smoothing weight. Chambolle smoothing only alters the distribution function meaningfully near the trapped-passing

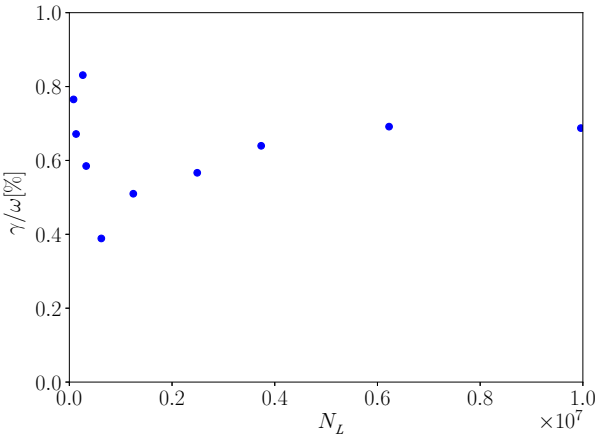

Figure 28: The linear growth rate normalised to the wave frequency, γ/ω, for the $n = 9$ TAE as a function of the number of beam ions used to calculate the distribution function in LOCUST, N_L.

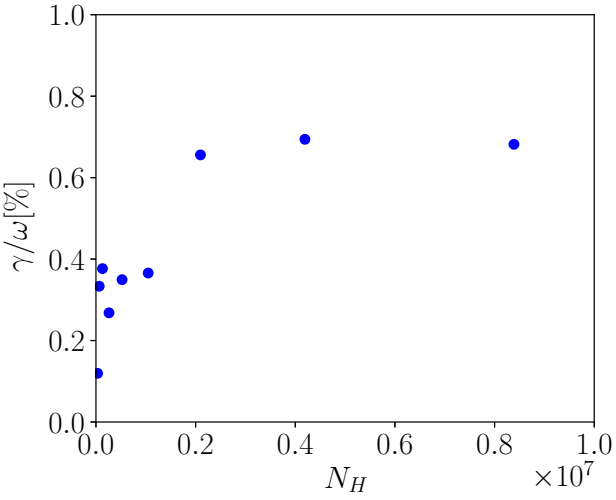

Figure 29: The linear growth rate of the $n = 9$ TAE of interest as a function of the number of beam ion markers used in HALO, N_H.

boundary in the counter-current direction, where it fixes the patch of singularity removal. However, only an arbitrarily small amount of smoothing must be used.

5 Conclusions

During steady, low power ($P_{NBI} = 11.6\ MW$) beam injection in our JET DT experiment, we observed high-frequency modes using two diagnostics, an interferometer and a reflectometer. These modes were observed at a frequency $f = 155\ kHz$, were located deep in the plasma $3.0 \leq R(m) \leq 3.4$ and exhibited chirping behaviour. Using the linear MHD code MISHKA, we identified these modes as TAEs. 21 TAEs with toroidal mode numbers $0 \leq n \leq 14$ fit experimental observations. We modelled beam ions and alpha particles using the full orbit particle tracking code LOCUST. Exploiting the latest GPU hardware to follow $\sim 10^7$ markers allows us to calculate a smooth, high-resolution distribution. The low statistical

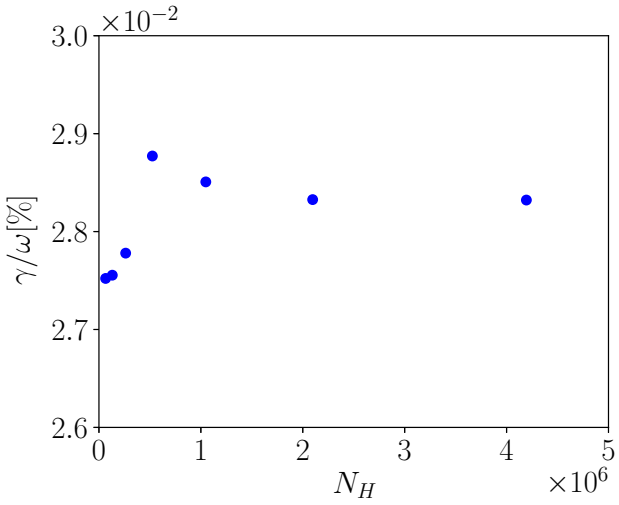

Figure 30: The linear growth rate of the $n = 9$ TAE of interest as a function of the number of alpha particle markers used in HALO, N_H.

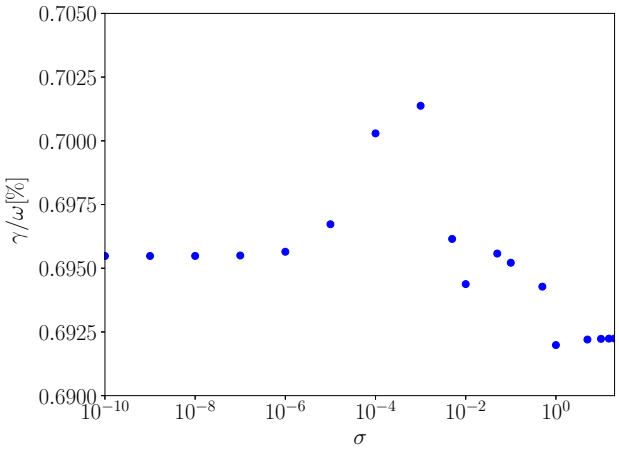

Figure 31: The linear growth rate of the $n = 9$ TAE of interest as a function of the Chambolle smoothing weight σ used to process the beam distribution function. The smoothing weight is multiplied by the maximum value of the distribution function.

noise in these distribution functions means it was possible to calculate mode stability without taking analytical fits of the distribution function, which is typically required to remove spurious gradients but removes important features of the distribution function including the trapped-passing boundary, the full, half and third energy beam injection, the magnetic axis boundary and even the $E \geq \mu B$ boundary.

We calculated the stability of the 21 candidate modes using the wave-particle interaction code HALO. These calculations revealed beam ions can drive TAEs with toroidal mode numbers $n \geq 8$, while TAEs with $n < 8$ were damped by the beam ion population. The maximum drive from beam ions is $\gamma_d/\omega \approx 1.0\%$. The surprising discovery that beam ions can drive high n TAEs in JET was supported by a simple analytical calculation of the ion diamagnetic frequency. The drive from alpha particles was also assessed. All but one of the candidate TAEs were weakly driven by alpha particles, with peak growth rates $\gamma_\alpha/\omega \approx 0.05\%$ due to the low alpha power generated in our experiment. Guiding centre

calculations were found to significantly overestimate growth rates compared to full orbit calculations for both beam and alpha particles.

Non-ideal damping effects were computed for each candidate mode using the CASTOR code. Radiative damping was found to be dominant, particularly for high m even modes, in agreement with previous calculations on JET [27]. However, collisional damping was also significant, particularly for modes in the outer half of the plasma. Continuum damping was weak for all modes. Ion Landau damping was calculated using a Maxwellian distribution function for thermal ions in HALO, but growth rates were small compared to radiative and collisional damping due to the low plasma temperature and high magnetic field.

Comparing the drive from energetic particles to damping from thermal particles, we found a single net-driven TAE with a net growth rate $\gamma/\omega = 0.02\%$. This TAE matches experimental observations with a frequency $f = 163kHz$ and location $R = 3.31m$. The marginally unstable growth rate calculated numerically matches the observation of chirping behaviour. The TAE was driven by co-passing particles due to P_ϕ gradients through the $v_\parallel = v_A/5$ resonance, with additional sideband resonances contributing significant drive.

A beam-driven mode is visible in our experiment due to a reduction in damping produced by the low electron temperature and high magnetic field. The drive was boosted by a relatively high safety factor profile and moderate beam power. The absence of ICRH made it easier to identify the source of the drive for the mode.

We assessed the dependence of the convergence of this calculation on the number of markers used in LOCUST and HALO. At least $6M$ beam markers were required in LOCUST calculations to capture all of the features of the distribution function in sufficient detail. Only $1M$ alpha particles were required to capture all physics due to the comparatively simpler alpha particle distribution function. HALO calculations required a minimum of $4M$ beam ions to resolve all features of the beam ion distribution function, while the alpha particle calculation only required $262K$ markers for a reliable result. We also checked the dependence of the linear growth rate on the processing of the distribution function. There was almost no change in the linear growth rate over seven orders of magnitude of the smoothing weight.

Acknowledgements

This work has been carried out within the framework of the EUROfusion Consortium, funded by the European Union via the Euratom Research and Training Programme (Grant Agreement No 101052200 — EUROfusion) and from the EPSRC [grant number EP/W006839/1]. Views and opinions expressed are however those of the author(s) only and do not necessarily reflect those of the European Union or the European Commission. Neither the European Union nor the European Commission can be held responsible for them. To obtain further information on the data and models underlying this paper please contact PublicationsManager@ukaea.uk*.

References

[1] C. Z. Cheng, L. Chen, and M. S. Chance. High-n ideal and resistive shear Alfvén waves in tokamaks. *Annals of Physics*, 161(1):21 – 47, 1985.

[2] F. Porcelli, R. Stankiewicz, W. Kerner, and H. L. Berk. Solution of the drift-kinetic equation for global plasma modes and finite particle orbit widths. *Physics of Plasmas*, 1(3):470–480, 1994.

[3] H. L. Berk, W. Horton, M. N. Rosenbluth, and P. H. Rutherford. Microinstability theory of two-energy-component toroidal systems. *Nuclear Fusion*, 15(5):819–844, 1975.

[4] J. A. Rome, D. G. McAlees, J. D. Callen, and R. H. Fowler. Particle-orbit loss regions and their effects on neutral-injection heating in axisymmetric tokamaks. *Nuclear Fusion*, 16(1):55, 1976.

[5] C. Di Troia. Bayesian derivation of plasma equilibrium distribution function for tokamak scenarios and the associated landau collision operator. *Nuclear Fusion*, 55(12):123018, 2015.

[6] M. Fitzgerald, S. E. Sharapov, P. Siren, E. Tholerus, M. Dreval, G. Szepesi, P. Vallejos, T. Johnson, N. Fil, J. Ferreira, P. Rodrigues, A. Figueiredo, D. Borba, R. Coelho, F. Nabais, J. Mailloux, H. J. C. Oliver, C. Di Troia, F. Napoli, Ž. Štancar, R. Dumont, D. Keeling, and JET Contributors. Toroidal Alfvén eigenmode stability in JET internal transport barrier afterglow experiments. *Nuclear Fusion*, 62(10):106001, 2022.

[7] D. Borba, H. L. Berk, B. N. Breizman, A. Fasoli, F. Nabais, S. D. Pinches, S. E. Sharapov, D. Testa, and contributors to the EFDA-JET Workprogramme. Modelling of Alfvén waves in JET plasmas with the CASTOR-K code*. *Nuclear Fusion*, 42(8):1029, 2002.

[8] R. J. Dumont, J. Mailloux, V. Aslanyan, M. Baruzzo, C. D. Challis, I. Coffey, A. Czarnecka, E. Delabie, J. Eriksson, J. Faustin, J. Ferreira, M. Fitzgerald, J. Garcia, L. Giacomelli, C. Giroud, N. Hawkes, Ph. Jacquet, E. Joffrin, T. Johnson, D. Keeling, D. King, V. Kiptily, B. Lomanowski, E. Lerche, M. Mantsinen, L. Meneses, S. Menmuir, K. McClements, S. Moradi, F. Nabais, M. Nocente, A. Patel, H. Patten, P. Puglia, R. Scannell, S. Sharapov, E. R. Solano, M. Tsalas, P. Vallejos, H. Weisen, and JET contributors. Scenario development for the observation of alpha-driven instabilities in JET DT plasmas. *Nuclear Fusion*, 58(8):082005, 2018.

[9] J. Seo, J. Kim, J. Mailloux, R. J. Dumont, M. Fitzgerald, S. E. Sharapov, D. L. Keeling, F. Koechl, F. J. Casson, C. Y. Lee, T. S. Hahm, Y. S. Na, and JET contributors. Parametric study of linear stability of toroidal Alfvén eigenmode in JET and KSTAR. *Nuclear Fusion*, 60(6):066008, 2020.

[10] S. E. Sharapov and et al. TBC. *to be submitted to Nuclear Fusion*, 2023.

[11] A. Boboc, L. Zabeo, and A. Murari. Simultaneous cotton-mouton and faraday rotation angle measurements on jet. *Review of Scientific Instruments*, 77(10):10F324, 2006.

[12] B. N. Breizman, H. L. Berk, and H. Ye. Collective transport of alpha particles due to Alfvén wave instability. *Physics of Fluids B: Plasma Physics (1989-1993)*, 5(9):3217–3226, 1993.

[13] S. Hacquin, S. E. Sharapov, B. Alper, C. D. Challis, A. Fonseca, E. Mazzucato, A. Meigs, L. Meneses, I. Nunes, S. D. Pinches, and the JET EFDA Contributors. Localized X-mode reflectometry measurements of Alfvén eigenmodes on the JET tokamak. *Plasma Physics and Controlled Fusion*, 49(9):1371, 2007.

[14] M. Dreval, S. E. Sharapov, Ye. O. Kazakov, J. Ongena, M. Nocente, R. Calado, R. Coelho, J. Ferreira, A. Figueiredo, M. Fitzgerald, J. Garcia, C. Giroud, N. C. Hawkes, V. G. Kiptily, F. Nabais, M. F. F. Nave, H. Weisen, T. Craciunescu, M. Salewski, Ž. Štancar, and JET Contributors. Alfvén cascade eigenmodes above the TAE-frequency and localization of Alfvén modes in D–3He plasmas on JET. *Nuclear Fusion*, 62(5):056001, 2022.

[15] L. L. Lao, H. St. John, R. D. Stambaugh, A. G. Kellman, and W. Pfeiffer. Reconstruction of current profile parameters and plasma shapes in tokamaks. *Nuclear Fusion*, 25(11):1611, 1985.

[16] M. Baruzzo, B. Alper, T. Bolzonella, M. Brix, P. Buratti, C. D. Challis, F. Crisanti, E. de la Luna, P. C. de Vries, C. Giroud, N. C. Hawkes, D. F. Howell, F. Imbeaux, E. Joffrin, H. R. Koslowski, X. Litaudon, J. Mailloux, A. C. C. Sips, O. Tudisco, and JET-EFDA contributors. Neoclassical tearing mode (NTM) magnetic spectrum and magnetic coupling in JET tokamak. *Plasma Physics and Controlled Fusion*, 52(7):075001, 2010.

[17] R. J. Hawryluk. An empirical approach to tokamak transport. In B. Coppi, G. G. Leotta, D. Pfirsch, R. Pozzoli, and E. Sindoni, editors, *Physics of Plasmas Close to Thermonuclear Conditions*, pages 19–46. Pergamon, 1981.

[18] G. T. A. Huysmans, J. P. Goedbloed, and W. Kerner. Isoparametric Bicubic Hermite Elements for Solution of the Grad-Shafranov Equation. *International Journal of Modern Physics C*, 02(01):371–376, 1991.

[19] G. T. A. Huysmans, S. E. Sharapov, A. B. Mikhailovskii, and W. Kerner. Modeling of diamagnetic stabilization of ideal magnetohydrodynamic instabilities associated with the transport barrier. *Physics of Plasmas*, 8(10):4292–4305, 2001.

[20] A. B. Mikhailovskii, G. T. A. Huysmans, W. O. K. Kerner, and S. E.. Sharapov. Optimization of computational MHD normal-mode analysis for tokamaks. *Plasma Phys. Rep.*, 23:844–857, 1997.

[21] R. J. Akers, E. Verwichte, T. J. Martin, S. D. Pinches, and R. Lake. GPGPU Monte Carlo Calculation of Gyro-Phase Resolved Fast Ion and n-State Resolved Neutral Deuterium Distributions. *39th EPS Conference and 16th Int. Congress on Plasma Physics*, P5.088:3217–3226, 2012.

[22] S. H. Ward, R. Akers, A. S. Jacobsen, P. Ollus, S. D. Pinches, E. Tholerus, R. G. L. Vann, and M. A. Van Zeeland. Verification and validation of the high-performance Lorentz-orbit code for use in stellarators and tokamaks (LOCUST). *Nuclear Fusion*, 61(8):086029, 2021.

[23] A. Pankin, D. McCune, R. Andre, G. Bateman, and A. Kritz. The tokamak Monte Carlo fast ion module NUBEAM in the National Transport Code Collaboration library. *Computer Physics Communications*, 159(3):157–184, 2004.

[24] E. Hirvijoki, O. Asunta, T. Koskela, T. Kurki-Suonio, J. Miettunen, S. Sipilä, A. Snicker, and S. Äkäslompolo. Ascot: Solving the kinetic equation of minority particle species in tokamak plasmas. *Computer Physics Communications*, 185(4):1310–1321, 2014.

[25] H. S. Bosch and G. M. Hale. Improved formulas for fusion cross-sections and thermal reactivities. *Nuclear Fusion*, 32(4):611, 1992.

[26] W. W. Heidbrink. Analytical expressions for fusion spectra produced in "beam - target" fusion reactions. *Review of Scientific Instruments*, 56(5):1098–1099, 1985.

[27] M. Fitzgerald, J. Buchanan, R. J. Akers, B. N. Breizman, and S. E. Sharapov. HALO: A full-orbit model of nonlinear interaction of fast particles with eigenmodes. *Computer Physics Communications*, 252:106773, 2020.

[28] R. E. Denton and M. Kotschenreuther. δf algorithm. *Journal of Computational Physics*, 119(2):283–294, 1995.

[29] A. Chambolle. An algorithm for total variation minimization and applications. *Journal of Mathematical Imaging and Vision*, 20:89–97, 2004.

[30] T. Fülöp, M. Lisak, Ya. I. Kolesnichenko, and D. Anderson. Finite orbit width stabilizing effect on toroidal Alfvén eigenmodes excited by passing and trapped energetic ions. *Plasma Physics and Controlled Fusion*, 38(6):811, 1996.

[31] R. R. Mett and S. M. Mahajan. Kinetic theory of toroidicity-induced Alfvén eigenmodes. *Physics of Fluids B: Plasma Physics (1989-1993)*, 4(9):2885–2893, 1992.

[32] J. W. Connor, R. O. Dendy, R. J. Hastie, D. Borba, G. Huysmans, W. Kener, and S. Sharapov. Non-ideal Effects on Toroidal Alfvén Eigenmode Stability. In Geneva EPS, editor, *Proceed. of 21st EPS Conference*, volume **18B**, page 616, 1994.

[33] P. Rodrigues, A. Figueiredo, J. Ferreira, R. Coelho, F. Nabais, D. Borba, N. F. Loureiro, H. J. C. Oliver, and S. E. Sharapov. Systematic linear-stability assessment of Alfvén eigenmodes in the presence of fusion α-particles for ITER-like equilibria. *Nuclear Fusion*, 55(8):083003, 2015.

[34] A. C. A. Figueiredo, P. Rodrigues, D. Borba, R. Coelho, L. Fazendeiro, J. Ferreira, N. F. Loureiro, F. Nabais, S. D. Pinches, A. R. Polevoi, and S. E. Sharapov. Comprehensive evaluation of the linear stability of Alfvén eigenmodes driven by alpha particles in an ITER baseline scenario. *Nuclear Fusion*, 56(7):076007, 2016.

[35] N. N. Gorelenkov and S. E. Sharapov. On the collisional damping of TAE-modes on trapped electrons in tokamaks. *Physica Scripta*, 45(2):163, 1992.

[36] F. Nabais, V. Aslanyan, D. Borba, R. Coelho, R. Dumont, J. Ferreira, A. Figueiredo, M. Fitzgerald, E. Lerche, J. Mailloux, M. Mantsinen, P. Rodrigues, M. Porkolab, P. Puglia, S. E. Sharapov, and JET Contributors. TAE stability calculations compared to TAE antenna results in JET. *Nuclear Fusion*, 58(8):082007, 2018.

[37] A. Hasegawa and L. Chen. Kinetic processes in plasma heating by resonant mode conversion of Alfvén wave. *Physics of Fluids (1958-1988)*, 19(12):1924–1934, 1976.

[38] G. W. Bowden, A. Könies, M. J. Hole, N. N. Gorelenkov, and G. R. Dennis. Comparison of methods for numerical calculation of continuum damping. *Physics of Plasmas*, 21(5):052508, 2014.

[39] Ž. Štancar and et al. Interpretive modelling of fusion performance in JET DTE2 discharges with TRANSP. In *64th Annual Meeting of the APS Division of Plasma Physic*, volume PO03.00012, 2022.